Catalysts by pyrolysis: Transforming metal-organic frameworks (MOFs) precursors into metal-nitrogen-carbon (M-N-C) materials

Ying Huang, Yechuan Chen, Mingjie Xu, Alvin Ly, Albert Gili, Eamonn Murphy, Tristan Asset, Yuanchao Liu, Vincent de Andrade, Carlo Segre, et al.

Catalysts by Pyrolysis: Transforming Metal-Organic Frameworks (MOFs) Precursors into Metal-Nitrogen-Carbon (M-N-C) Materials

Ying Huang[1,2†], Yechuan Chen[2,3†], Mingjie Xu[1,4], Alvin Ly[1,2], Albert Gili[5], Eamonn Murphy[2,3], Tristan Asset[2,3], Yuanchao Liu[2,3], Vincent De Andrade[6], Carlo U. Segre[7], Alex L. Deriy[6], Francesco De Carlo[6], Martin Kunz[8], Aleksander Gurlo[5], Xiaoqing Pan[1,4], Plamen Atanassov[2,3*], Iryna V. Zenyuk[1,2,3*]

1 Department of Materials Science & Engineering, University of California Irvine, CA 92697, USA
2 National Fuel Cell Research Center, University of California Irvine, CA 92697, USA
3 Department of Chemical & Biomolecular Engineering, University of California Irvine, CA 92697, USA
4 Irvine Materials Research Institute, University of California Irvine, CA 92697, USA
5 Fachgebiet Keramische Werkstoffe/Chair of Advanced Ceramic Materials, Institut für Werkstoffwissenschaften und-technologien, Technische Universität Berlin, Hardenbergstr. 40, 10623 Berlin, Germany
6 Advanced Photon Source, Argonne National Laboratory, 9700 South Cass Avenue, Lemont, IL 60439, USA
7 Department of Physics and CSRRI, Illinois Institute of Technology, Chicago, IL, 60616, USA
8 Advanced Light Source, Lawrence Berkeley National Laboratory, CA 94720, USA
† These authors contributed equally
*Corresponding authors: plamen.atanassov@uci.edu, Iryna.zenyuk@uci.edu

Abstract

Metal-organic framework (MOF) materials are promising precursors to transition into metal-nitrogen-carbon (M-N-C) catalysts with high catalytic performance. Pyrolysis is one of the most common ways to convert MOFs into electrically conductive MOF-derived M-N-C catalysts. General interests in using MOFs as precursors derive from changing the MOFs' porous structure into the carbonaceous frame. However, this favorable structure is not always maintained, with the reason unidentified since pyrolysis is currently still more of an empirical process. Understanding the pyrolysis processes leading to the transformation of MOFs into M-N-C catalysts is essential to broaden the development of MOF-derived catalysts. We report here complete chemical and morphological evolution and transformation of two commercial MOFs with the same sodalite topology, the ZIF-8 and ZIF-67, *via* series of *in situ* and *ex situ* techniques. The results reveal that the structure of the ZIF-67 collapses after the pyrolysis due to the graphitization of the carbon. Graphitization is catalyzed by the metallic cobalt particles formed when the temperature rose above 460 °C. The ZIF-8 was found to be a promising precursor material since most of the metal evaporates at the early stages and does not aggregate to form metal particles. However, the insufficient metal-N active sites and intrinsic low electrocatalysis availability of Zn limit the performance of the final catalyst. To maintain the porous structure of MOFs it is important to control the metal species and prevent them from agglomeration. Direct utilization of high-concentration MOFs as pyrolysis precursors is not recommended without rational design to inhibit agglomeration and graphitization that are undesirable for catalyst activity.

Keywords

Pyrolysis, Oxygen reduction reaction, Transition metal-nitrogen-carbon electrocatalysts, Metal-organic frameworks, Catalysts synthesis

Introduction

Hydrogen technology is central for the decarbonization of heavy-duty transportation sector, difficult to directly electrify manufacturing as well as enable long-duration energy storage. When converted to electricity in polymer electrolyte fuel cells (PEFCs) no greenhouse gas emissions are generated and the only byproduct is water. For widespread adoption of PEFCs, their stack cost needs to be reduced. In the frame of large-scale development, Pt catalyst is considered as the largest portion of the stack cost[1]. Most of the Pt loading is on the cathode side, where oxygen reduction reaction (ORR) takes place. Substantial efforts have been made to develop PGM-free catalysts, among which the pyrolyzed metal-nitrogen-carbon (M-N-C) being one of the most promising alternatives to the PGM materials[2-8].

Metal-nitrogen moieties ($M\text{-}N_x$) embedded in the carbon matrix of M-N-C materials have been recognized as the most essential active sites in ORR[9-12]. Significant efforts have been made to atomically disperse the metal species in the carbon matrix in order to obtain a higher density of active sites, as overall catalyst activity is proportional to electrochemically accessible site density. Besides the $M\text{-}N_x$ sites, rationally designed carbonaceous materials are also necessary for the M-N-C catalysts, as their porous space ensures gaseous permeability and liquid-phase accessibility and the solid-state framework provides electronic conductivity and, through its surface properties, proton conductivity as well. The most common approach is obtaining M-N-C catalysts with sufficient $M\text{-}N_x$ sites and specialty carbonaceous materials is pyrolyzing the mixture of metal-, nitrogen- and carbon-containing precursors. Typical materials reported as precursors are macrocyclic compounds[13,14], polymers[15-17], metal-organic frameworks (MOFs)[4,18] and the mixture of the above with templating agents[3,5]. Among these candidates, MOF-derived catalysts show great potential for high catalytic activity, which comes from the porous structure with high surface areas and periodic metal-nitrogen-carbon bonds. Zeolitic imidazolate framework (ZIF) materials are usually the selected MOF precursors to synthesize M-N-C catalysts. Previous studies showed that the half-wave potential for the ORR of the catalysts synthesized from iron-doped ZIF-8 with a surface area of 969 $m^2\ g^{-1}$ reached 0.82 V in acidic media[19]. The catalysts derived from Co-based MOF with a surface area of 1359 $m^2\ g^{-1}$ exhibit a half-wave potential of around 0.85 V in alkaline media[20]. Recently, a great deal of effort has been made to disperse the metal on ZIF-8 materials by using chemical vapor deposition (CVD) during pyrolysis. With CVD, iron salt vapor can

be transported over ZIF-8 derived Zn-N-C materials, transmetalating the Zn sites with Fe, yielding a Fe-N-C catalyst with well-dispersed Fe-N_4 sites[21]. CVD was also conducted to deposit N-doped carbon on the prepared Fe-N-C catalysts, yielding highly stable pyridinic N-coordinated Fe-N_4 sites, significantly improving the durability of the catalyst[22].

General interest in pyrolyzing MOFs to synthesize catalysts is based on the hypothesis that the favorable porous structure of MOFs can be sustained during heat treatment. The high porosity and the surface area of the structure facilitates molecular transport and provides the possibility for the active sites to be highly dispersed. However, the above hypothesis might not always be correct. Some synthesized M-N-C catalysts derived from MOF-based materials and their corresponding morphological information, as well as the ORR activity in the acid electrolyte, are summarized in Supplementary Material (Table S1). From the (scanning) transmission electron microscopy images in previous studies[20,23], the hexagonal shape of the MOFs observed by microscopy before the pyrolysis did not persist after the pyrolysis.

Despite a large number of original and review publications, there is no specific study of chemical and morphological changes of MOF pyrolytic transformations. Moreover, critical details of such synthesis are seldom omitted in reporting or even misrepresented. There is widespread confusion as many claim the "chemical templating nature of MOFs" while others report very active MOF-derived catalysts with no structural resemblance to the precursor. The technical reason why pyrolyzed precursors only partially maintain their original MOF structure remains unclear. The pyrolysis process is currently a "Pandora's box" – the structure of the product is only revealed after the synthesis process. Recently, several studies started to dedicate efforts to reveal the relationship between the pyrolysis temperature and catalysts' properties and their performance. It was found that the porphyrin-like ZnN_4 site could form when temperature reached 600 °C[24] and high temperature would lead the ZIF-8 from crystalline structure to porous carbon structure[25]. However, the extent to which the morphological properties affect the electrochemical performance of MOF-derived catalysts remains ambiguous. These factors hinder the rational design of MOF-based catalysts. Herein, we observed the pyrolysis of the MOF materials by a combination of *in situ* and *ex situ* techniques to reveal the transformation from the morphological and spectroscopic perspective. Two commercial ZIFs with the same structures (ZIF-8 named Basolite® Z1200 from Sigma-Aldrich© and ZIF-67 from PlasmaChem©) were selected as MOF precursors in the study. ZIF-8, coordinated with zinc ions, and ZIF-67, coordinated with cobalt ions, share the same tetrahedral imidazole ligand coordination and sodalite topology. ZIF-8 (Figure 1a) has been combined with other precursors to form good transition metal-N-C catalysts[23,24,26-28]. ZIF-67 (Figure 1d) can be used as a sole precursor since it contains cobalt, carbon and nitrogen in the same source. Ideally, cobalt is expected to bond with nitrogen and form Co-N_x active sites after pyrolysis[20,29,30]. With commercial chemicals,

fewer interfering factors, like unknown contaminations and unexpected operation errors, are involved. Thus, the pathway of MOF leading to the carbonaceous materials *via* pyrolysis can be better characterized. The direct observation and thorough analysis of "the birth of catalysts" would be the foundation for the rational design of M-N-C.

Results and Discussion

As verified by X-ray diffraction (XRD), ZIF-8 (Figure 1b) and ZIF-67 (Figure 1e) are both pure crystalline products. The pattern of the ZIF-8 correlates rigorously with the structure reported by Yaghi's group[31]. In the pattern of the ZIF-67, extra peaks were observed at $2\theta_{8\ keV} \approx 37.8°$, 39.6°, and 46.1° (X-ray energy was converted to 8 keV from 25 keV based on Bragg's law) compared to the standard simulated XRD pattern structure[32]. These peaks might correspond to $Co(OH)_2$ (PDF# 00-030-0443) and CoN (PDF# 01-083-8039), which was probably in coexistence with the cobalt source materials used to synthesize the ZIF-67 and will be further discussed in the *in situ* XRD results. Thermogravimetric analysis (TGA) was performed to examine the sample mass changes during pyrolysis. The derivative thermogravimetry (DTG) profile reveals transforming temperature points, which were later used as observation points for *in situ* experiments. For ZIF-8, the DTG curve shows a sharp peak at 625 °C, which should be due to the ZIF-8 melting and decomposition[33]. We also observed the loss of Zn component under the STEM (discussed later); thus, the mass loss can also be caused by the Zn component evaporation. The sample mass of the ZIF-8 kept decreasing after 625 °C and did not reach a plateau. The DTG curve of ZIF-67 exhibits continuous peaks from around 490 °C to 615 °C. This should correspond to ZIF-67 melting and decomposition[34,35].

The pyrolysis step is critical for converting MOFs into M-N-C catalysts, and often leads to severe morphological transformations. *In situ* scanning transmission electron microscopy (STEM) experiments that were performed under a vacuum environment reveal the change of the precursor morphology within a selected field of view. In the pristine images of the ZIF-8, hexagonal facets were clearly observed (Figure 2a and Figure S1). The corresponding energy-dispersive X-ray spectroscopy (EDS) indicates that Zn, N, and C are all distributed uniformly (Figure S2). When the temperature was elevated, the overall geometry of the materials did not show apparent changes but the size shrinkage (Figure 2a and Figure S3). With image thresholding, the percentage change of the area of ZIF-8 shown in the STEM from all temperatures can be quantified. The captured area of the materials in the region of interest (ROI) decreased by 34.7% at 650 °C and then by 45.2% at 850 °C compared to the pristine (Table S2). Only half of the area of the material remained in the ROI after the pyrolysis process. The EDS mapping shown in Figure S8 reveals very little of the Zn existence after pyrolysis. A zoom-in ROI at different temperatures showing a hexagonal facet of the ZIF-8 is also provided (Figure S4-S7). The structure became loose and more

porous when the temperature was elevated to 650 °C. At 850 °C, the structure transformed into a more fibrous and disordered state, and turbostratic carbon as well as some clusters appeared as Figure S6 shows. After the sample was pyrolyzed to 1050 °C and after cooling down, the structure became more hollow together with numerous bright "dots" indicating the formation of metal clusters over the carbon substrate. These clusters and bright dots are most likely zinc species (according to EDS results in Figure S8-S9). The changes of the materials in three-dimensional views are further revealed via *in situ* nano-CT experiments under nitrogen environment. No noticeable transformation was observed before 650 °C. When comparing the volume of an ROI calculated based on the segmentation results, the materials shrank by 23.8% (Table S3 and Figure S10). This is consistent with the 600 °C results gained from thresholding STEM images as provided in Table S2a. More representative cross-section images from the *in situ* nano-CT experiments are found in the SI (Figure S11-S12).

Crystal structure transformations were observed by performing *in situ* XRD experiment during the pyrolysis. The evolution patterns of ZIF-8 were collected at the rate of 10 °C min^{-1} and under a flowing gas stream composed of 5% H_2 and 95% Ar (Figure 2c and Figure S13). The atmosphere contains hydrogen to remove oxygen and avoid oxidation, essentially providing a reducing environment. Based on catalytic performance of the samples pyrolyzed in different atmospheres reported in the previous publication[5,36,37], the hydrogen fraction should not provide enough chemical potential to significantly change the pyrolysis process when comparing the samples pyrolyzed in pure Ar/N_2. Note that all intensity peaks at elevated temperatures are shifted toward lower 2θ compared to the reference patterns due to thermal expansion and corresponding increase of d-spacing. All diffraction peaks related to pristine MOF structure started disappearing at around 520 °C, indicating decomposition or amorphization. With the temperature elevated to 640 °C, the signal disappeared, and only flat patterns remained (as shown in Figure S14 for zoomed 24°-30° 2θ region). Interestingly, there was a diffraction peak at $2\theta \approx 21.5°$ appearing at 970 °C, which later disappeared during the sample cooling down. This diffraction pattern belongs to α-cristobalite ($P4_12_12$, PDF# 00-039-1425), belonging to the sample-containing SiO_2 capillary, and thus is an artifact from sample preparation. This artifact was confirmed by comparison with the *ex situ* data of the pyrolyzed ZIF-8 (Figure S15), where this pattern was not observed, indicating that the SiO_2 is not inside the samples. This artifact should not affect the conclusion since the results from the XRD were consistent with the observation from other characterizations. No other new diffraction appeared when comparing the final pattern with the pristine one, confirming that no extra crystalline structure but totally amorphous product was formed during the pyrolysis. The process of amorphization at the lower temperature can be better demonstrated by the relative crystallinity changes as a function of temperature in ZIF-8 (Figure S16). The relative crystallinity of ZIF-8 was reduced to 53% around 600 °C. This number further decreased to zero at around 640 °C, indicating that the sample was fully

amorphized[38]. The decrease in the relative crystallinity can be attributed to the local Zn-N_4 tetrahedron deformation, meaning that the long-range-order structure has been transformed into the short-range-order one.

To obtain more information about the structural changes, *ex situ* XAS at the Zn K-edge was measured on the ZIF-8 pyrolyzed to 650 °C, 850 °C, 980 °C, and 1050 °C under Ar atmosphere. The pronounced peaks at 1.55Å in Zn K-edge R space plots (Figure 2d) can be assigned to the Zn-N shell. It revealed that some Zn remained in the sample after pyrolysis, and they are bonded with N to form Zn-N_x sites (coordination number x=4.5±0.5, detailed fitting information in Table S4, Figure S17). The XANES data (Figure 2e and Figure S18) of pristine ZIF-8 shows features at 9666.1 eV and 9673.7 eV, which should be associated with tetrahedral Zn-N_4. The former feature appears due to the Zn 1*s* → Zn 4*p* transitions, while the latter feature reflects the multiple scattering of the mid-range order structure[12,39,40]. After pyrolysis, a peak at ca. 9669 eV showed up as the only feature, which indicates the existence of Zn-N_4 (D_{4h} symmetry). This feature shifted to lower energy when comparing the sample at 650 °C to those at higher temperatures. This change was caused by the variation in the degree of distortion of the D_{4h} symmetry. Given the fact that square planar Zn-N_4 should cause a peak at around 9667 eV, the above phenomenon indicates that Zn^{2+} were sitting closer to the porphyrin-like N_4 plane when the temperature increased[41].

Ex situ Raman spectroscopy was performed to understand the evolution of MOFs to carbonaceous materials. The ZIF-8 samples pyrolyzed to 650 °C, 850 °C, 980 °C, and 1050 °C under Ar atmosphere were measured (Figure 2f and Figure S20, Table S5). The sample pyrolyzed to 650 °C has not fully transformed into carbonaceous material; thus, the corresponding Raman spectrum is complicated by the bands assigned to methyl group vibration, D band, and G+D' band[42,43]. The G band comes from the vibration of the E_{2g} symmetry of the ideal graphitic lattice while the D' band comes from the vibration of the E_{2g} symmetry of disordered graphitic lattice. D' band always appeared as a shoulder of G band and here they were fitted together. When the samples were pyrolyzed to 850 °C, 980 °C, and 1050 °C, the corresponding Raman signal can then be convolved into four peaks associated with G+D' band (~1593 cm^{-1}), distorted carbon (~1504 cm^{-1}), D band (~1346 cm^{-1}) and the sp^2 carbon outside of the graphene network (~1220 cm^{-1}) (Figure S19)[43,44]. The increased peak intensity at ~1220 cm^{-1} suggests that the carbon matrix of the sample pyrolyzed to 980 °C contains higher out-of-the-plane carbon compared to the sample pyrolyzed to a lower temperature. Once the temperature reached 980 °C, further elevating the pyrolysis temperature did not have much effect on the carbon matrix. The ratio of the intensities of the D band and G+D' band are both around 1.35 of the ZIF-8 pyrolyzed to 980 °C and 1050 °C (Figure S19d).

From the morphological and structural characterizations of the ZIF-8 and its pyrolyzed products, the pyrolyzed ZIF-8 can be an excellent soft template for the M-N-C catalysts. It overall retains the favorable

porous structure of MOF (which would be confirmed with N_2 absorption in later discussion), contains carbon mainly with an open structure, and its metal element did not agglomerate but spread out uniformly on the matrix. The ZIF-8 pyrolyzed to 980 °C and 1050 °C should have similar performance in terms of being an N-C precursor for metal deposition for ORR, if there were no further catalytic graphitization triggered by extra mixture components. This performance could be probably attributed to the relatively inert behavior of Zn.

Compared to zinc, cobalt is a livelier transition metal element. Similar characterizations have been carried out to study the transformation of ZIF-67 during pyrolysis (Figure 3). *In situ* STEM experiments reveal the morphological transformation of the ZIF-67 during pyrolysis at the nanoscale, showing a thoroughly different behavior with Zn as described previously. Hexagonal facets were clearly shown in the 250 °C images (Figure 3a and Figure S20). Corresponding EDS indicates that Co, N, and C are all distributed uniformly (Figure S21-22). However, when the temperature reached 450 °C, metallic species started agglomerating violently and forming clusters of ~20 nm (Figure 3a and Figure S23-24). These metal nanoclusters further grew into large clusters of ~100 nm during the pyrolysis (Figure S25). The EDS taken after the pyrolysis confirmed that the clusters mainly consist of cobalt (Figure S26). The melting point and the vaporization point of the cobalt are over 1500 °C when the vapor pressure is higher than 1×10^{-7} atm[45]. The Co evaporation temperature would increase if there was a gas atmosphere existing and the pressure was lower. Based on the empirical equation $\log p = -2.5(10^4/T) + 9.5$, the vapor pressure around 1000 K could be simply estimated as 3×10^{-16} atm discarding phase change. This value is several orders smaller than the ultra-high vacuum (1×10^{-7} Pa or 1×10^{-12} atm) environment inside STEM setup[45]. Thus, after ZIF-67 melted and decomposed, the cobalt stayed in the solid state in our experiment. At more elevated temperatures, cobalt clusters further migrated due to the heating. Several clusters aggregated to decrease surface energy and become stable, leading to cluster size growth[46]. The cobalt clusters started catalyzing the carbon graphitization once the temperature reached over 1000 °C[47,48]. The porous structure thus collapsed due to the carbon graphitization, which should result in the surface area decrease (discussed later with N_2 absorption results). From the STEM, the carbon phase in the pyrolyzed product was combined with the graphitic carbon and the amorphous carbon (Figure S25). Some of the graphitic carbon wrapped the metal particle as the heterogeneous catalysis occurred on the interface between cobalt and carbon, making the cobalt particle difficult to be removed by the acid etching, and causing decreased porosity in the final product. The STEM images showed the precursor material area after pyrolysis inside an ROI decreased by 58.1% compared to the one pyrolyzed up to 250 °C (Table S6). *In situ* nano-CT experiments under nitrogen environment further revealed the changes of the materials in three dimensions. The volume of the same ROI decreased from around 148.4 μm^3 to 45.7 μm^3, which corresponds to percentage volume change of 69.2% after the temperature

increased from 200 °C to 980 °C (Figure S27 and Table S7). More corresponding cross-section images from the *in situ* nano-CT experiments are shown in the SI (Figure S28-29).

The *in situ* XRD experiment of ZIF-67 was performed with a heating rate of 10 °C min^{-1} and under flowing 5% H_2 and 95% Ar atmosphere (Figure 3c and Fig. S30-S34). Note that all diffractions are shifted toward lower 2θ compared to the reference patterns due to thermal expansion. All 2θ were reported based on the X-ray energy of 8 keV (converted from 25 keV based on Bragg's law). The main diffraction of ZIF-67 (011) at $2\theta_{8\ keV} \approx 7.30°$ disappeared at 446 °C, which is consistent with the aforementioned melting and decomposition point from the TGA result (Fig. 1f). The peaks at $2\theta_{8\ keV} \approx$ 37.8°, 39.6°, and 46.1° are assigned to $Co(OH)_2$ (PDF# 00-030-0443) and CoN (PDF# 01-083-8039), as byproducts during the synthesis of this commercial ZIF-67 product. The ZIF-67 occupied 65.4 wt.% while CoN occupied 26.7 wt.% according to the fitting results (Figure S31). With the temperature further elevated, $Co(OH)_2$ decomposed. The diffraction at $2\theta_{8\ keV} \approx 43.9°$ appeared when the samples pyrolyzed to 467 °C, and the one at $2\theta \approx 50.8°$ became pronounced above 625 °C. These peaks are assigned to cubic Co (111) and (200), respectively (PDF# 00-015-0806). The diffraction at $2\theta_{8\ keV} \approx 47.0°$ and 41.1° can be assigned to hexagonal Co (PDF# 04-007-8518), which is not thermally stable above 450 °C (Figure S32) and probably transformed to the cubic structure at higher temperature[49,50]. CoN (PDF# 01-083-8039), which appeared in the precursor's spectrum, was still present after pyrolysis. The diffraction at $2\theta_{8\ keV} \approx$ 21.8°, which also appeared in the ZIF-8 spectrum, can be attributed to α-cristobalite ($P4_12_12$, PDF# 00-039-1425) belonging to the quartz capillary for sample holding. The *ex situ* measurement of the ZIF-67 pyrolyzed at 1050 °C did not detect this feature (Figure S35), suggesting that the sample did not include SiO_2. The signal at $2\theta_{8\ keV} \approx 26.4°$ that appeared at approximately 992 °C with a crystallite size of around 0.36 nm (FWHM=0.3820) corresponds to the graphite (002) diffraction (PDF# 00-041-1487) (Figure S36). After the pyrolysis, the crystal structure of ZIF-67 transformed to mainly metallic Co (48.2 wt.%) and some cobalt nitrite (15.5 wt.%) existed according to the fitting results (Figure S33 and S34). The metallic Co catalyzed the graphitization process, causing the carbon matrix to be destroyed. This phenomenon has also been observed in a previous study[48]. Besides Co, Fe[51] and other metals[52] can also catalyze the graphitization during pyrolysis process. Even though graphitic carbon can enhance the electrical conductivity of the final product, microporosity of the materials is also important for an ORR catalyst to reach a good performance[53]. The graphitization caused the collapse of the porous structure and decreased surface proton conductivity. One of the main reasons to use MOF as precursor materials is MOF holds a favorable porous structure, and the heavy graphitization process weakens the advantage.

Ex situ XAS at the Co K-edge was measured on the ZIF-67 pyrolyzed to 450 °C, 650 °C, 850 °C, and 1050 °C under Ar atmosphere. The most pronounced peak at 1.55Å in the FT-EXAFS of the pristine ZIF-

67 is associated with the Co-N bonding, as shown in Figure 3d. After the sample was pyrolyzed, the features at 2.21Å related to the Co-Co shell became dominant (Figure 3d, detailed fitting information in Figure S37, and Table S8). This correlates with the appearance of the metal particles in the STEM images and XRD patterns. The XANES data (Figure 3e and Figure S38) of pristine ZIF-67 demonstrates features at 7710 eV and 7728 eV. The former one is associated with the Co 1*s* → 3*d* transition, while the latter one is associated with the Co 1*s* → 4*p* transition[54]. The data of pristine ZIF-67 included a sharper peak arising from the white line compared to the data of the sample pyrolyzed to 450 °C. This indicates that the Co was in the oxidation state of +2. This could be from the ZIF-67 itself[55]. Combining the results from XRD, this can also be from the $Co(OH)_2$ existing in the pristine ZIF-67[56,57]. When the sample was pyrolyzed to 650 °C and above, the XANES spectra demonstrated the same features revealing the metallic Co particles in the samples[58].

Ex situ Raman spectroscopy was utilized to understand the evolution of MOF to carbonaceous materials (Figure 3f and Figure S39, and D/G ratio information in Table S9). Similar to that of low-temperature treated ZIF-8, the spectrum of the sample pyrolyzed to 450 °C demonstrates the features corresponding to the methyl group vibration, as well as the D band and G+D' band. The samples pyrolyzed to 650 °C and above can be considered carbonaceous materials. The intensity of the G+D' band increased as the temperature raised. The ratio of the intensities of the D band and G+D' band in the sample pyrolyzed to 1050 °C is less than one, indicating that more graphitic carbon exists than the defected or disordered carbon in the materials. These results agree with the conclusion from *in situ* STEM and XRD experiments. It is also worth noticing that the spectrum of the sample pyrolyzed to 1050 °C contains a sharp D' band (~ 1615 cm^{-1}) (Figure S39). This means more defected-induced graphitic features (armchair or zigzag edge in the graphitic carbon structure[59]) existed in the samples. The appearance of the sharp D' band indicates that a significant amount of graphitic carbon exists in the samples pyrolyzed to 1050 °C.

From the morphological and structural characterizations of the ZIF-67 and its pyrolyzed products, the pyrolyzed ZIF-67 lost the favorable porous structure of MOF. The reason that the structure collapsed was the carbon graphitization, which was catalyzed by the Co cluster that formed during the pyrolysis. In our case, the final product of pyrolysis of ZIF-8 had no metallic particle and thus catalyzed graphitization was not observed. This phenomenon indicates that other transition metals which were reported to have catalytic graphitization availability, including iron, nickel, *etc.*, might cause the same issue, if they remain in the matrix and agglomerate. The cobalt-catalyzed graphitization process is due to heteroepitaxial growth. The carbon solubility is 3.41% atom in Co at 1000 °C[60]. This means that carbon easily diffused into the bulk Co. As a consequence, Co precipitated a significant amount of carbon onto its surface, and thus the graphitic carbon formed[61]. Also, Co has a strong interaction with graphene[62],

meaning that the graphitic carbon layers (which are multiple layers of graphene) could be attached to the Co particle surface firmly. On the other hand, due to the existence of the cobalt nanoparticles, the pyrolyzed product of ZIF-67 might have a high peroxide yield during ORR, which is confirmed later with the electrochemical testing results.

To learn more about the evolution of the surface chemistry and to confirm the porous network structures evolution envisaged from the previous STEM results, the samples pyrolyzed to 975 °C were acid-etched to remove the particles (scheme was described in Figure 4a-b). The samples were not pyrolyzed above 1000 °C to avoid the formation of excess graphitic carbon, which might cause difficulties in removing particles (Figure S40 shows the example where Co particles remained inside the graphite layer after acid etching). XPS was performed to understand the surface chemistry of the precursors (ZIF-8 and ZIF-67), the samples pyrolyzed to 975 °C, and the samples before and after acid etching (Figure 4c-d, Table S10-S11). Ar-etching technique was applied to reveal the chemistry of the content beneath the surface. The surface chemistry changes mainly occurred during the pyrolysis process. The atomic concentration of the C 1s on the ZIF-8 sample surface increased by 30.7% after pyrolysis, while the N 1*s* and the Zn 2*p* decreased by 76.1% and 92.1%, separately. The decrease of the Zn 2*p* atomic concentration confirms that the metal species evaporated during the heat treatment. After acid etching, the atomic concentration on the sample surfaces of Zn 2*p* further decreased and the O 1*s* increased slightly. This indicates that some of the metal species etched away, and the surface adsorbed some water during the etching. The atomic concentrations of C 1*s*, N 1*s* and Zn 2*p* did not change, meaning that the contents are uniform on the sample surface. For the ZIF-67, the atomic concentration of the C 1*s* has similar changes as the ZIF-8 sample after pyrolysis and acid etching. The atomic concentration of O 1*s* did not change significantly on ZIF-67 surface after pyrolysis and decreased a little bit after the acid-etching. However, there was a large decrease in the N 1*s* and Co 2*p* concentrations on the surface of the ZIF-67. Most of the nitrogen and Co might be beneath the sample surface in a collapsed structure. The high-resolution C 1*s* and N 1*s* XPS spectra with curve fitting reveal the carbon framework and N moiety composition (Figure S41-46). The typical M-N-C carbon framework appeared after the samples were pyrolyzed. Metal-N is the most favorable site since it prefers the four-electron pathway[63]. The atomic concentration of metal-N in the pyrolyzed ZIF-67 increased by 66.3% after Ar etching. This indicates that most of the cobalt is embedded inside the samples. Pyridine N and N-H (including pyrrolic N and hydrogenated pyridinic N) are favorable for the first and second steps of the two-electron pathway[63]. The ratio of these above sites is related to the efficiency of this pathway. The ratio was close to one for the acid-etched pyrolyzed ZIF-8. However, the ratio of the pyrolyzed ZIF-67 before and after acid-etching was 0.87 and 0.78, respectively. Inductively coupled plasma-mass spectrometry (ICP-MS) was also performed to assess the quantity of the metal element inside the final catalysts before and after acid etching. The zinc in pyrolyzed ZIF-8 was

0.52 wt.% while the number decreased to 0.27 wt.% after acid etching. The cobalt in pyrolyzed ZIF-67 was 64.98 wt.% while the number dramatically was reduced to 1.80 wt.% after acid etching.

N_2 absorption was applied to probe the changes in the pyrolyzed product before and after the acid etching step. The isotherms of the ZIF-8 samples showed abrupt increases at low relative pressure (Figure 4e). This indicates the existence of micropores. There was no significant difference in the surface area and the pore size distribution of the samples after acid etching (surface area: 1,171.8 $m^2 g^{-1}$) compared to the one before (surface area: 1,219.9 $m^2 g^{-1}$). Thus, the acid etching did not affect significantly the pyrolyzed ZIF-8 zinc samples. The isotherms of the ZIF-67 samples displayed typical type-IV isotherms with a type H4 hysteresis loop in the range of $P/P0 > 0.4$, indicating the presence of mesopores. The sample after acid etching showed a higher surface area (surface area: 158.0 $m^2 g^{-1}$) and increased pore volume (Figure S47) compared to the one before etching (surface area: 51.8 $m^2 g^{-1}$). This can be due to the removal of the cobalt nanoparticles.

The electrochemical activity of the samples pyrolyzed at different temperatures was assessed with a rotating ring disk electrode setup (summary in Figure 4f, detailed information in Figure S48-S55). Overall, the cyclic voltammetry (CV) curves of the samples pyrolyzed to higher temperatures demonstrated a quasi-rectangular shape. The capacitance of the ZIF-8 pyrolyzed to 1050 °C, as shown in Figure S50, was lower than the ones pyrolyzed at 850 °C and 980 °C, which indicates an eventual collapse of the pristine porous structure. This phenomenon can also be attributed to the existence of more disordered graphitic carbon and the decreased volume of pores. The half-wave potential of the ZIF-8 pyrolyzed to 1050 °C, although very similar to the one of the samples pyrolyzed to 980 °C as shown in Figure S52, is the highest. This is probably due to the metal-N active sites formation at high temperatures. For ZIF-67, the sample pyrolyzed to 450 °C had a very low capacitance, indicating that the carbon substrate had not formed at this stage. With the pyrolysis temperature increased, the capacitance first increased and then decreased. That is due to the existence of metallic cobalt, which blocked some of the pores in the sample. The half-wave potential of the pyrolyzed ZIF-8 is higher than the pyrolyzed ZIF-67, disregarding the high degree of graphitization of the pyrolyzed ZIF-67. This reflects that the degree of graphitization is not the governing factor of good performance. However, the half-wave potential of the pyrolyzed ZIF-67 increased from 0.48 V to 0.61 V after acid etching, while the half-wave potential of the pyrolyzed ZIF-8 remained roughly the same. This is due to the increase of the capacitance and of the surface area after the removal of the metal particles. The peroxide yield of the pyrolyzed ZIF-67 is much higher compared to the pyrolyzed ZIF-8 no matter whether it was acid etched or not. The reason is that the product of pyrolyzed ZIF-67 contained more inactive metallic cobalt (embedded in the carbon structure) and probably cobalt carbide. This led to the insufficient existence of the $M\text{-}N_x$ sites in the

sample, which can further reduce the peroxide to water. Thus, the pyrolyzed ZIF-67 could not efficiently reduce the peroxide, which generation was catalyzed by the N-H sites in the final catalysts. The same conclusion can be drawn from the experiments performed under both 1600 rpm and 900 rpm.

Combining all the characterization results, the transformation from the MOF precursors to the M-N-C catalysts was directly observed. The most pronounced difference between the pyrolyzed product of ZIF-8 and ZIF-67 was the formation of the metallic particles (Figure 5). The metallic particles, though can be active for the ORR, would not be dispersed well during the pyrolysis and thus the metal active site density was low. Furthermore, the Co particles catalyzed the carbon graphitization process easily during the pyrolysis process due to the high carbon solubilities in cobalt. As contrast, the most crucial advantage of ZIF-8 being a precursor is the well-dispersed Zn after the pyrolysis process. However, the Zn concentration inside the sample was low since this element could evaporate and sublimate (metallic Zn boils around 550 °C or sublimates around 300 °C at low pressure[64]) at the early stage of the pyrolysis. This indicates that not many metal-related active sites exist in the final catalysts but retained porous carbon matrix with decent N-C moieties. This significantly affects the performance, resulting in a low 0.6 V half-wave potential in acid but high peroxide yield. Thus, ZIF-8 has the promise to be a great templating precursor for ORR, as it can serve as a template for deposition of transition metal species, such as Fe that are active towards ORR[21,22,65].

In conclusion, MOF has a favorable porous structure that benefits catalytic activity. To make it conductive and to form M-N-C catalysts, pyrolysis is an essential and convenient step. However, pyrolyzing transition metal-doped MOFs can cause the formation of severely agglomerated particles. This formation not only significantly decreases the concentration of the active sites but also catalyzes carbon graphitization at high temperatures. The graphitization process causes the favorable structure to collapse, and thus voids the meaning of applying MOF as precursors. Direct heat treatment utilization of high-concentration transition metal MOFs towards carbonaceous electrocatalyst synthesis would not be recommended unless specific rational designs are developed to inhibit potential agglomeration and graphitization. ZIF-8 is a more promising MOF precursor candidate since its doping metal, Zn, evaporates and sublimes during the pyrolysis, thus it did not trigger catalytic graphitization during heat treatment and retains the porous structure. However, its limited electrocatalytic performance requires the involvement of other metal elements and improvement strategies. The possible synergetic effects between Zn and other metals in multi-metal MOFs during synthesis for electrocatalysis still remain uncertain. It is critical to note that transition nano-particles formation during pyrolysis plays the role of switching the molecular templating of MOF structure towards solid-state templating by the nascent metal/metal carbide/ metal oxide nanophase.

Methods

Materials synthesis

ZIF-8 was purchased from Sigma-Aldrich© (Basolite® Z1200), while ZIF-67 was purchased from PlasmaChem©. The *ex situ* samples were pyrolyzed with a ramping rate of 10 °C min^{-1} under Ar. The acid etched products were prepared by etching the pyrolyzed samples with 3M HCl overnight followed by being washed with deionized water until the pH reached neutral values.

Scanning transmission electron microscope (STEM)

The *in situ* heating STEM experiments were done in a vacuum environment. The Protochips Fusion Select™ was used where there is one heating chip (E-FHDC, Protochips, Inc.) applied and the $\varphi = 8$ μm holes were covered by holey carbon thin films. The MOF materials were dispersed in the ethanol solvent with ultrasound bath. The resulting sample suspension was then dropped onto the heating chip by pipette. After the sample had dried on the chip, an optical microscope was used to check whether the powder sample was on the chip windows.

The sample for *ex situ* STEM experiments was dispersed in ethanol solvent by ultrasound bath. The resulting suspension was then dropped on the holey carbon-coated copper grid. The sample was dried before transferring into the STEM.

STEM was performed on a JEOL JEM-ARM300CF microscope with probe correctors and a 300 kV cold field emission gun. All reported temperatures were calculated by the measured electrical resistance of the heater. Energy dispersive X-ray spectroscopy (EDS) was collected at the pristine state, 250 °C, and at the final cooling-down state, with 100 mm^2 dual silicon drift detectors.

In situ X-ray nano-computed tomography (nano-CT)

The *in situ* heating X-ray nano-CT experiments were performed with the transmission X-ray microscope from beamline 32-ID of the Advanced Photon Source (APS) at Argonne National Laboratory (ANL). Monochromatic X-rays of 8 keV energy were applied. A 50 nm outermost zone width Fresnel zone plate was used as an objective lens and a phase-ring placed in the back focal plane of the zone plate was used to perform imaging in Zernike phase contrast mode. The resulting voxel size is 21.3 nm.

Samples were mounted on the graphite pin, which was mounted onto a high-accuracy air-bearing rotary stage. The top part of the pin was enveloped by an inductive furnace with X-ray transparent window. The N_2 gas flew through the furnace during the whole experiment. Scans were performed for pyrolysis process at pristine state, 200 °C, 400 °C, 600 °C, 850 °C, 980 °C, 1050 °C and at the final state after cooling down to room temperature. However, the images taken at high temperatures were not reconstructed since the rotating center was changing during the scan due to the intense vibrations. The temperature stepping ramp rate was used with 10 °C s^{-1} and 15 min hold time at each temperature.

The data was reconstructed with TomoPy and ASTRA toolbox[66-68,69]. Image processing was done with Dragonfly 2022.1 Software (Object Research Systems (ORS) Inc, Montreal, Canada; software available at http://www.theobjects.com/dragonfly). The semantic segmentation is done with UNet++ architecture[70,71].

X-ray diffraction (XRD)

The *ex situ* XRD is performed on Rigaku SmartLab with Cu Kα source. High-temperature *in situ* powder XRD was collected at beamline 12.2.2 of the Advanced Light Source (ALS) at Lawrence Berkeley National Laboratory (LBNL) in an environmental cell previously reported[72-76]. Around 1 mg of the powder sample was introduced into a 0.7 mm outer diameter quartz capillary provided by Hilgenberg GmbH, Germany. The gas was delivered by a set of mass flow controllers to the sample *via* a tungsten carbide injection capillary. The quartz capillary and the tungsten carbide capillary were both mounted and enclosed inside a silicon carbide cylinder with two holes allowing X-ray beam to pass. The cylinder was heated with two infrared lamps (Osram 64635HLX) and served as a furnace. A pattern with a LaB_6 standard NIST 660b was acquired for setup calibration before the experiment. The setup temperature was controlled using a S-type thermocouple placed next to the sample. Prior to performing experiments with the MOF samples, a temperature calibration curve was done using Pt as standard material all along the temperature range. The reported temperature was the average temperature during a 30 s exposure time. All experiments were performed with an incident X-ray beam of 25 keV and a spot size of 30 × 30 μm^2.

The XRD data was collected when the precursor material was heated from room temperature to 1035 °C at the rate of 10 °C min^{-1}, held at 1035 °C for 30 min, and cooled to room temperature under 5% H_2 and 95% Ar atmosphere. The gas was flowing at 10 NmL min^{-1}. The patterns containing Debye diffraction rings were processed on-the-fly using Dioptas software[77] to yield intensity as a function of 2 Theta. The relative crystallinity was calculated by integrating area under the peaks and compared the integration to the one calculated based on the pristine spectrum. PDXL software was also used to analyze the data.

Thermogravimetric analysis (TGA)

TGA characterization was performed on a simultaneous thermal analyzer (Netzsch STA 449 F3 Jupiter). The precursor materials were mounted in ceramic crucibles. Blank experiments were performed for background corrections. All samples were heated under Ar from 80 °C to 1020 °C with the rate of 10 °C·min^{-1}. NETZSCH Proteus Thermal Analysis was used to analyze the data.

Raman spectroscopy

The Raman spectra were obtained on a Horiba LabRAM HR Evolution confocal Raman microscope with 633 nm laser and 600 g mm^{-1} grating. 100x objective was applied. Twenty-five individual 20 s spectra were accumulated. CasaXPS software was used to analyze the data. All data was fitted with four peaks based on publications[42,44].

X-ray Absorption Spectroscopy (XAS)

XAS data were collected at the 10-BM beamline of APS at ANL [78]. The sample was mixed with some binder and pressed as a pellet. The pellet was then sealed in a holder with Kapton tapes. The products of pyrolyzed ZIF-8 were measured at the Zn K-edge (9659 eV) in transmission mode. The products of pyrolyzed ZIF-67 were measured at Co K-edge (7709 eV) in fluorescence mode. The data was processed and modeled using the Demeter XAS software package[79]. The EXAFS amplitude reduction factor S_0^2 was determined based on the fitting of standard reference material. The fits were performed in k-weight = 1,2,3 with a Fourier Transform range and fitting window indicated in Table S3 and S6.

X-ray Photoelectron Spectroscopy (XPS)

XPS was performed on a Kratos AXIS Supra spectrometer with a monochromatic Al Kα source. Ar ion cluster was used to etch the sample surface for 30 s with 500 eV Ar250+ cluster setup after the surface was characterized. CasaXPS software was used to analyze the data. The fitting was using 70% Gaussian / 30% Lorentzian setup based on previous calculations and publications[16,63,80-83].

Inductively Coupled Plasma-Mass Spectrometry (ICP-MS)

ICP-MS was mearsured on the ThermoFisher iCAP RQ ICP-MS system. The powder samples were digested in aqua regia over several days, and then diluted to ppb concentration levels in 1 vol.% nitric acid in Milli-Q water. The standard calibration curves were prepared by diluting an elemental standard in 1 vol.% nitric acid in Milli-Q water and then performing a series of auto-dilutions in the system.

Nitrogen physisorption

Nitrogen physisorption was done in a Micromeritics 3Flex Surface and Catalyst Analyzer. The samples were vacuumed at 90 °C for 1 h and then at 200 °C for 6 h before the measurement. The surface area was calculated by the Barrett-Emmett-Teller (BET) method. The pore size distribution was obtained with the non-local density functional theory model (NLDFT).

Electrochemical measurement

The electrochemical experiments were done with a rotating ring disk electrode (RRDE) setup. The catalyst inks (9.88 $\mu g \cdot \mu L^{-1}$) were prepared by mixing samples, 5 wt.% Nafion solution (Sigma-Aldrich) and 1:1 MilliQ H_2O (18.2 MΩ) / Isopropanol (Sigma-Aldrich) under sonication. 2 × 10 µL of the catalyst ink was drop cast on the working electrode (glassy carbon electrode, $S_{geo} = 0.247$ cm^2 with a platinum ring) while the electrode was rotating slowly. The electrode was dried under heat-flux (and while maintaining rotation) between each deposition. A final layer of 800 µg cm^{-2} loadings was derived. The catalyst was activated in an N_2-saturated electrolyte through 100 cycles at 500 mV s^{-1} between 0.05 and 1.23 V vs. RHE, followed by 3 cycles at 20 mV s^{-1} and linear sweep voltammetry between 0.05 and 1.05 V vs. RHE at 20 mV s^{-1} (as a baseline correction). Then, linear sweep voltammetry between 0.05 and 1.05 V vs. RHE at 20 mV s^{-1} was measured at 900 rpm and 1600 rpm at O_2-saturated electrolyte. The data was corrected from the ohmic losses in solution and the baseline obtained in N_2-saturated electrolyte.

Acknowledgment

IVZ would like to acknowledge support from the National Science Foundation under CBET Award 1605159. This research used the resources of the Advanced Light Source (ALS). The ALS is supported by the Director, Office of Science, Office of Basic Energy Sciences, of the U.S. Department of Energy under Contract No. DE-AC02-05CH11231. This research used resources of the Advanced Photon Source, a U.S. Department of Energy (DOE) Office of Science User Facility operated for the U.S. DOE

Office of Science by Argonne National Laboratory under contract No. DE-AC02-06CH11357. XAS was performed in the Materials Research Collaborative Access Team (MRCAT). MRCAT operations are supported by the Department of Energy and the MRCAT member institutions. STEM, XRD (SmartLab), ICP-MS and TGA were performed at the UC Irvine Materials Research Institute (IMRI). XPS was performed at the UC Irvine Materials Research Institute (IMRI) using instrumentation funded in part by the National Science Foundation Major Research Instrumentation Program under grant no. CHE-1338173. Raman was conducted in UC Irvine's Horiba Institute for Mobility and Connectivity^2 (HIMAC^2).

Data Availability

The raw data is available to be shared upon request from the authors.

Reference

1. James, B. D., Fuel Cell Systems Analysis In *2021 DOE Hydrogen and Fuel Cells Program Review Presentation*, (2021)
2. Lefèvre, M., *et al.*, *Science* (2009) **324** (5923), 71, https://doi.org/10.1126/science.1170051
3. Serov, A., *et al.*, *Electrochimica Acta* (2013) **109**, 433, https://doi.org/https://doi.org/10.1016/j.electacta.2013.07.104
4. Strickland, K., *et al.*, *Nature Communications* (2015) **6** (1), 7343, https://doi.org/10.1038/ncomms8343
5. Serov, A., *et al.*, *Nano Energy* (2015) **16**, 293, https://doi.org/10.1016/j.nanoen.2015.07.002
6. Chung, H. T., *et al.*, *Science* (2017) **357** (6350), 479, https://doi.org/10.1126/science.aan2255
7. Li, J., *et al.*, *Nature Catalysis* (2018) **1** (12), 935, https://doi.org/10.1038/s41929-018-0164-8
8. Cui, X., *et al.*, *Advanced Functional Materials* (2021) **31** (10), 2009197, https://doi.org/https://doi.org/10.1002/adfm.202009197
9. Kramm, U. I., *et al.*, *Physical Chemistry Chemical Physics* (2012) **14** (33), 11673, https://doi.org/10.1039/c2cp41957b
10. Tylus, U., *et al.*, *The Journal of Physical Chemistry C* (2014) **118** (17), 8999, https://doi.org/10.1021/jp500781v
11. Zitolo, A., *et al.*, *Nature Materials* (2015) **14** (9), 937, https://doi.org/10.1038/nmat4367
12. Jia, Q., *et al.*, *ACS Nano* (2015) **9** (12), 12496, https://doi.org/10.1021/acsnano.5b05984
13. Cook, A. H., *Journal of the Chemical Society (Resumed)* (1938), 1761, https://doi.org/10.1039/jr9380001761
14. Jasinski, R., *Nature* (1964) **201** (4925), 1212, https://doi.org/10.1038/2011212a0
15. Wu, G., *et al.*, *Science* (2011) **332** (6028), 443, https://doi.org/10.1126/science.1200832
16. Artyushkova, K., *et al.*, *ACS Applied Energy Materials* (2019) **2** (8), 5406, https://doi.org/10.1021/acsaem.9b00331
17. Ma, R., *et al.*, *Nano Energy* (2023) **108**, 108179, https://doi.org/https://doi.org/10.1016/j.nanoen.2023.108179
18. Proietti, E., *et al.*, *Nature Communications* (2011) **2** (1), 416, https://doi.org/10.1038/ncomms1427
19. Wang, H.-Y., *et al.*, *Journal of the American Chemical Society* (2016) **138** (1), 36, https://doi.org/10.1021/jacs.5b10525

20. Xia, W., *et al.*, *Nano Letters* (2017) **17** (5), 2788, https://doi.org/10.1021/acs.nanolett.6b05004
21. Jiao, L., *et al.*, *Nature Materials* (2021) **20** (10), 1385, https://doi.org/10.1038/s41563-021-01030-2
22. Liu, S., *et al.*, *Nature Energy* (2022) **7** (7), 652, https://doi.org/10.1038/s41560-022-01062-1
23. Wang, H., *et al.*, *Nano Energy* (2020) **77**, 105304, https://doi.org/https://doi.org/10.1016/j.nanoen.2020.105304
24. Wang, Q., *et al.*, *Science Bulletin* (2020) **65** (20), 1743, https://doi.org/https://doi.org/10.1016/j.scib.2020.06.020
25. Xiao, J.-D., *et al.*, *Journal of Catalysis* (2022) **406**, 165, https://doi.org/https://doi.org/10.1016/j.jcat.2021.12.033
26. Chen, X., *et al.*, *Applied Catalysis B: Environmental* (2020) **267**, 118720, https://doi.org/https://doi.org/10.1016/j.apcatb.2020.118720
27. Chen, M., *et al.*, *ACS Catalysis* (2020) **10** (18), 10523, https://doi.org/10.1021/acscatal.0c02490
28. Karapinar, D., *et al.*, *Angewandte Chemie International Edition* (2019) **58** (42), 15098, https://doi.org/10.1002/anie.201907994
29. Xia, W., *et al.*, *J. Mater. Chem. A* (2014) **2** (30), 11606, https://doi.org/10.1039/c4ta01656d
30. Zhang, M., *et al.*, *Advanced Materials* (2018) **30** (10), 1705431, https://doi.org/10.1002/adma.201705431
31. Park, K. S., *et al.*, *Proceedings of the National Academy of Sciences* (2006) **103** (27), 10186, https://doi.org/10.1073/pnas.0602439103
32. Banerjee, R., *et al.*, *Science* (2008) **319** (5865), 939, https://doi.org/doi:10.1126/science.1152516
33. Nozari, V., *et al.*, *Nature Communications* (2021) **12** (1), 5703, https://doi.org/10.1038/s41467-021-25970-0
34. Hu, Y., *et al.*, *RSC Advances* (2019) **9** (18), 9962, https://doi.org/10.1039/c9ra00874h
35. Han, X., *et al.*, *Energy & Fuels* (2021) **35** (5), 4447, https://doi.org/10.1021/acs.energyfuels.0c03878
36. Workman, M. J., *et al.*, *ACS Energy Letters* (2017) **2** (7), 1489, https://doi.org/10.1021/acsenergylett.7b00391
37. Reshetenko, T., *et al.*, *Electrochemistry Communications* (2020) **118**, 106795, https://doi.org/10.1016/j.elecom.2020.106795
38. Venna, S. R., *et al.*, *Journal of the American Chemical Society* (2010) **132** (51), 18030, https://doi.org/10.1021/ja109268m
39. Rossi, G., *et al.*, *Physical Chemistry Chemical Physics* (2016) **18** (34), 23686, https://doi.org/10.1039/c6cp04022e
40. Dadlani, A., *et al.*, *ACS Applied Materials & Interfaces* (2017) **9** (45), 39105, https://doi.org/10.1021/acsami.7b06728
41. Li, F., *et al.*, *Nature Communications* (2019) **10** (1), 2623, https://doi.org/10.1038/s41467-019-10622-1
42. Tanaka, S., *et al.*, *The Journal of Physical Chemistry C* (2015) **119** (51), 28430, https://doi.org/10.1021/acs.jpcc.5b09520
43. Sadezky, A., *et al.*, *Carbon* (2005) **43** (8), 1731, https://doi.org/10.1016/j.carbon.2005.02.018
44. Wu, G., *et al.*, *ACS Nano* (2012) **6** (11), 9764, https://doi.org/10.1021/nn303275d
45. Wachi, F. M., and Gilmartin, D. E., *The Journal of Chemical Physics* (1972) **57** (11), 4713, https://doi.org/10.1063/1.1678140
46. Akhtar, M. K., *et al.*, *Aerosol Science and Technology* (1994) **21** (1), 83, https://doi.org/10.1080/02786829408959698
47. Fu, R., *et al.*, *Langmuir* (2005) **21** (7), 2647, https://doi.org/10.1021/la047344d
48. Goldie, S. J., *et al.*, *Materials Advances* (2021) **2** (10), 3353, https://doi.org/10.1039/d1ma00125f
49. Nishizawa, T., and Ishida, K., *Bulletin of Alloy Phase Diagrams* (1983) **4** (4), 387, https://doi.org/10.1007/BF02868089

50. Sewak, R., *et al.*, *Scientific Reports* (2022) **12** (1), 10054, https://doi.org/10.1038/s41598-022-14302-x
51. Zhao, J., *et al.*, *Proceedings of the National Academy of Sciences* (2014) **111** (44), 15641, https://doi.org/10.1073/pnas.1412962111
52. Ōya, A., and Ōtani, S., *Carbon* (1979) **17** (2), 131, https://doi.org/https://doi.org/10.1016/0008-6223(79)90020-4
53. Wassner, M., *et al.*, *Beilstein Journal of Nanotechnology* (2020) **11**, 1, https://doi.org/10.3762/bjnano.11.1
54. Pattengale, B., *et al.*, *Journal of the American Chemical Society* (2016) **138** (26), 8072, https://doi.org/10.1021/jacs.6b04615
55. SantaLucia, D. J., *et al.*, *Inorganic Chemistry* (2022) **61** (16), 6056, https://doi.org/10.1021/acs.inorgchem.2c00066
56. Deng, T., *et al.*, *Nature Communications* (2017) **8** (1), 15194, https://doi.org/10.1038/ncomms15194
57. Gajdek, D., *et al.*, *The Journal of Physical Chemistry C* (2022) **126** (7), 3411, https://doi.org/10.1021/acs.jpcc.1c10284
58. Cheng, G., *et al.*, *Chemical Physics Letters* (2004) **400** (1), 122, https://doi.org/https://doi.org/10.1016/j.cplett.2004.10.095
59. Malard, L. M., *et al.*, *Physics Reports* (2009) **473** (5), 51, https://doi.org/https://doi.org/10.1016/j.physrep.2009.02.003
60. Sung, C.-M., and Tai, M.-F., *International Journal of Refractory Metals and Hard Materials* (1997) **15** (4), 237, https://doi.org/https://doi.org/10.1016/S0263-4368(97)00003-6
61. Dahal, A., and Batzill, M., *Nanoscale* (2014) **6** (5), 2548, https://doi.org/10.1039/C3NR05279F
62. Eom, D., *et al.*, *Nano Letters* (2009) **9** (8), 2844, https://doi.org/10.1021/nl900927f
63. Artyushkova, K., *et al.*, *The Journal of Physical Chemistry C* (2015) **119** (46), 25917, https://doi.org/10.1021/acs.jpcc.5b07653
64. Kaye, G. W. C., *et al.*, *Proceedings of the Royal Society of London. Series A, Containing Papers of a Mathematical and Physical Character* (1913) **89** (607), 58, https://doi.org/10.1098/rspa.1913.0063
65. Li, J., *et al.*, *Journal of the American Chemical Society* (2020) **142** (3), 1417, https://doi.org/10.1021/jacs.9b11197
66. De Carlo, F., *et al.*, *Journal of synchrotron radiation* (2014) **21** (6), 1224,
67. Gürsoy, D. A., *et al.*, *Journal of Synchrotron Radiation* (2014) **21** (5), 1188, https://doi.org/10.1107/s1600577514013939
68. Pelt, D. M., *et al.*, *Journal of Synchrotron Radiation* (2016) **23** (3), 842, https://doi.org/10.1107/s1600577516005658
69. De Andrade, V., *et al.*, *Advanced Materials* (2021) **33** (21), 2008653, https://doi.org/https://doi.org/10.1002/adma.202008653
70. Zhou, Z., *et al.*, UNet++: A Nested U-Net Architecture for Medical Image Segmentation. Springer International Publishing(2018), pp 3
71. Zhou, Z., *et al.*, *IEEE Transactions on Medical Imaging* (2020) **39** (6), 1856, https://doi.org/10.1109/TMI.2019.2959609
72. Kunz, M., *et al.*, *Journal of Synchrotron Radiation* (2005) **12** (5), 650, https://doi.org/doi:10.1107/S0909049505020959
73. Doran, A., *et al.*, *Review of Scientific Instruments* (2017) **88** (1), 013903, https://doi.org/10.1063/1.4973561
74. Schlicker, L., *et al.*, *Review of Scientific Instruments* (2018) **89** (3), 033904, https://doi.org/10.1063/1.5001695
75. Hardy, D. A., *et al.*, *Chemistry of Materials* (2019) **31** (19), 8163, https://doi.org/10.1021/acs.chemmater.9b02957
76. Bekheet, M. F., *et al.*, *ACS Catalysis* (2021) **11** (1), 43, https://doi.org/10.1021/acscatal.0c04290

77. Prescher, C., and Prakapenka, V. B., *High Pressure Research* (2015) **35** (3), 223, https://doi.org/10.1080/08957959.2015.1059835
78. Kropf, A. J., *et al.*, The New MRCAT (Sector 10) Bending Magnet Beamline at the Advanced Photon Source. AIP10.1063/1.3463194
79. Ravel, B., and Newville, M., *Journal of Synchrotron Radiation* (2005) **12** (4), 537, https://doi.org/doi:10.1107/S0909049505012719
80. Artyushkova, K., *et al.*, *Chemical Communications* (2013) **49** (25), 2539, https://doi.org/10.1039/c3cc40324f
81. Matanovic, I., *et al.*, *The Journal of Physical Chemistry C* (2016) **120** (51), 29225, https://doi.org/10.1021/acs.jpcc.6b09778
82. Matanovic, I., *et al.*, *Current Opinion in Electrochemistry* (2018) **9**, 137, https://doi.org/https://doi.org/10.1016/j.coelec.2018.03.009
83. Chen, Y., *et al.*, *ACS Applied Energy Materials* (2018) **1** (11), 5948, https://doi.org/10.1021/acsaem.8b00959

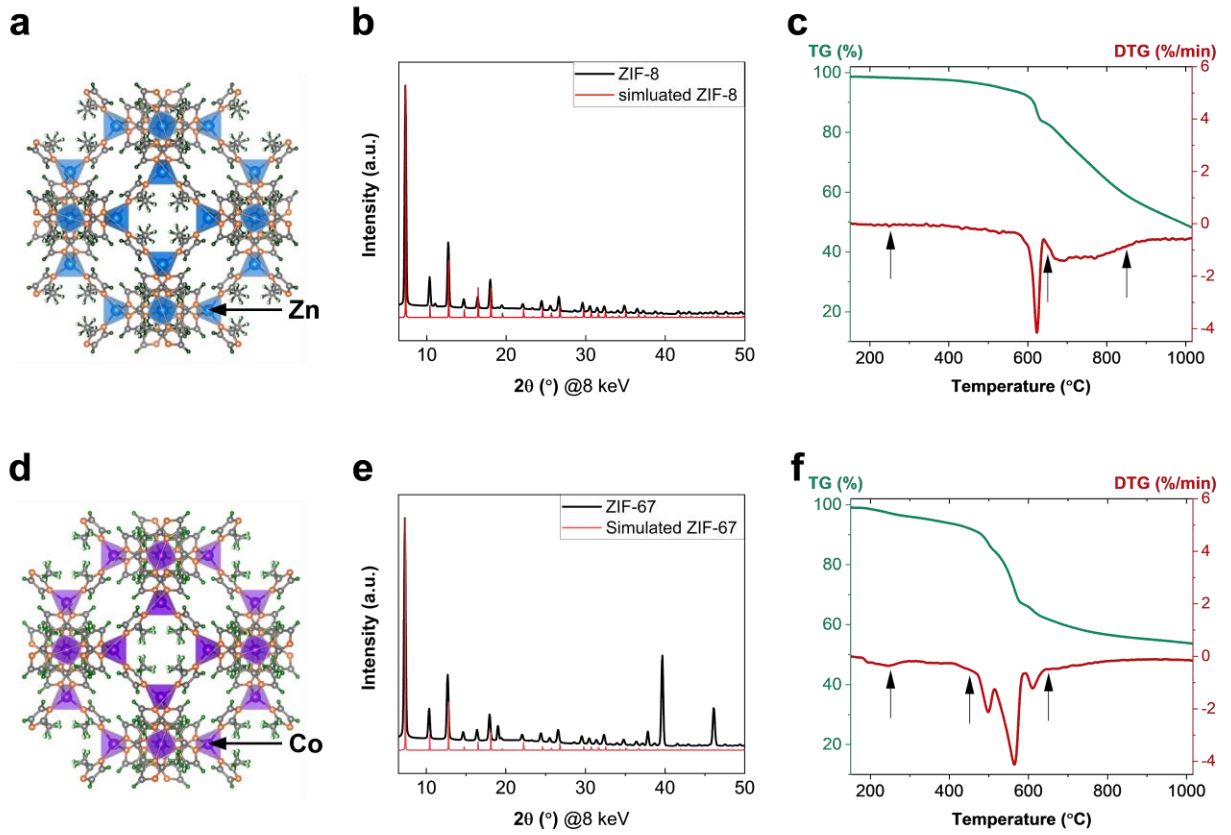

Figure 1. Characterization of the ZIF-8 and ZIF-67.

a. the crystal structure of ZIF-8

b. X-ray diffraction patterns of ZIF-8 and simulated pattern (CCDC-602542). The X-axis of the pristine ZIF-8 data has been converted from 25 keV (0.4959 Å) to Cu Kα (1.5406 Å).

c. TGA profile of ZIF-8 under Ar atmosphere. Arrows show the temperature points during the process chosen to be studied in the *in situ* STEM experiment

d. the crystal structure of ZIF-67

e. X-ray diffraction patterns of ZIF-67 and simulated pattern (CCDC-671073). The X-axis of the pristine ZIF-67 data has been converted from 25 keV (0.4959 Å) to Cu Kα (1.5406 Å).

f. TGA profile of ZIF-67 under Ar atmosphere. Arrows indicate the temperature points during the process chosen to be studied in the *in situ* STEM experiment

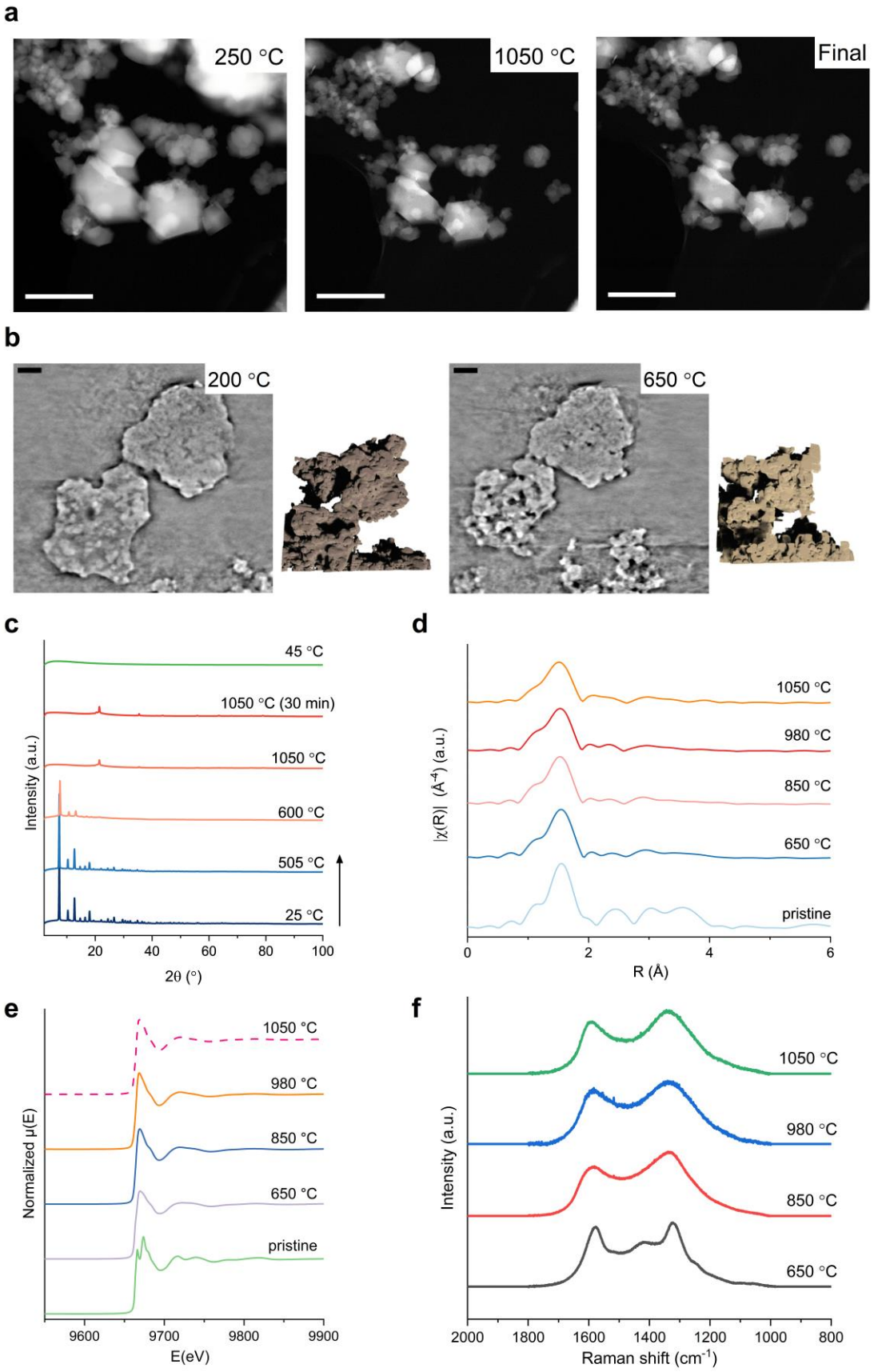
a
250 °C
1050 °C
Final
b
200 °C
650 °C
c
45 °C
1050 °C (30 min)
1050 °C
600 °C
505 °C
25 °C
Intensity (a.u.)
2θ (°)
d
1050 °C
980 °C
850 °C
650 °C
pristine
|χ(R)| (Å⁻⁴) (a.u.)
R (Å)
e
1050 °C
980 °C
850 °C
650 °C
pristine
Normalized μ(E)
E(eV)
f
1050 °C
980 °C
850 °C
650 °C
Intensity (a.u.)
Raman shift (cm⁻¹)

Figure 2. *In-situ* transformation of the ZIF-8 during pyrolysis.

a. *In situ* STEM experiment under vacuum. HAADF-STEM images for ZIF-8 during pyrolysis at 250 °C, 1050 °C and after cold down. Scale bar: 500 nm.

b. *In situ* nano-CT experiment under N_2 environment. Grayscale images and the three-dimensional volume renderings of the identical location of ZIF-8 during pyrolysis at 200 °C and 650 °C. Scale bar: 1,000 nm.

c. *In situ* XRD experiment under flowing 5% H_2 + 95% Ar. XRD patterns of ZIF-8 recoded at selected temperatures. The X-axis has been converted from 25 keV (0.4959 Å) to Cu Kα (1.5406 Å). The arrow indicates the reaction progress.

d. *Ex situ* EXAFS of the ZIF-8 and ZIF-8 pyrolyzed at 650 °C, 850 °C, 980 °C and 1050 °C under Ar environment.

e. *Ex situ* XANES of the ZIF-8 and ZIF-8 pyrolyzed at 650 °C, 850 °C, 980 °C and 1050 °C under Ar environment.

f. *Ex situ* Raman of the ZIF-8 pyrolyzed at 650 °C, 850 °C, 980 °C and 1050 °C under Ar environment.

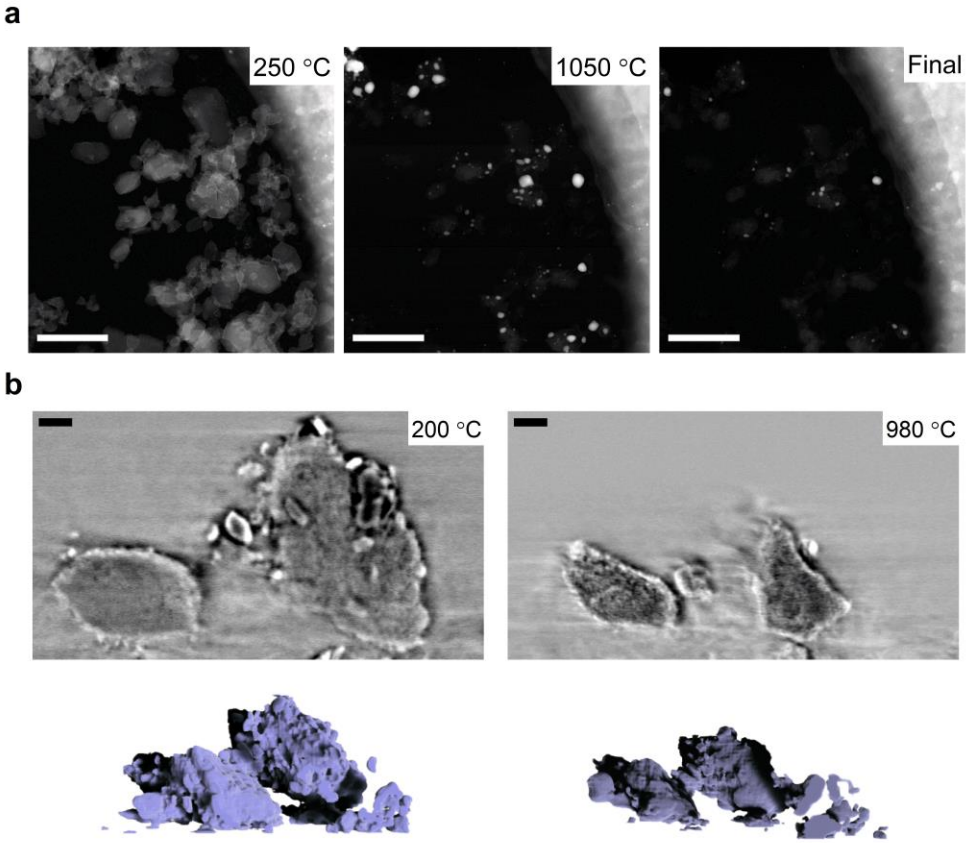
a
250 °C
1050 °C
Final
b
200 °C
980 °C
c
T (°C)
48
1050
(30 min)
1050
733
484
26
Intensity (a.u.)
2θ (°)
d
1050 °C
850 °C
650 °C
450 °C
pristine
|χ(R)| (Å⁻⁴) (a.u.)
R (Å)
e
1050 °C
850 °C
650 °C
450 °C
pristine
Normalized μ(E)
E(eV)
f
1050 °C
850 °C
650 °C
450 °C
Intensity (a.u.)
Raman shift (cm⁻¹)

Figure 3. Transformation of the ZIF-67 during pyrolysis.

a. *In situ* STEM experiment under vacuum. HAADF-STEM images for ZIF-67 during pyrolysis at 250 °C, 1050 °C and after cold down. Scale bar: 500 nm.

b. *In situ* nano-CT experiment under N_2 environment. Grayscale images and the three-dimensional volume renderings of identical location of the ZIF-8 during pyrolysis at 200 °C and 980 °C are shown. Scale bar: 1,000 nm.

c. *In situ* XRD experiment under flowing 5% H_2 + 95% Ar. XRD patterns of ZIF-67 recoded at selected temperatures. ♠ represents Co, ● represents CoN. The X-axis has been converted from 25 keV (0.4959 Å) to Cu kα (1.5406 Å). The arrow indicates the reaction progress.

d. *Ex situ* EXAFS of the ZIF-67 and ZIF-67 pyrolyzed at 450 °C, 650 °C, 850 °C and 1050 °C under Ar environment.

e. *Ex situ* XANES of the ZIF-67 and ZIF-67 pyrolyzed at 450 °C, 650 °C, 850 °C and 1050 °C under Ar environment.

f. *Ex situ* Raman of the ZIF-67 pyrolyzed 450 °C, 650 °C, 850 °C and 1050 °C under Ar environment.

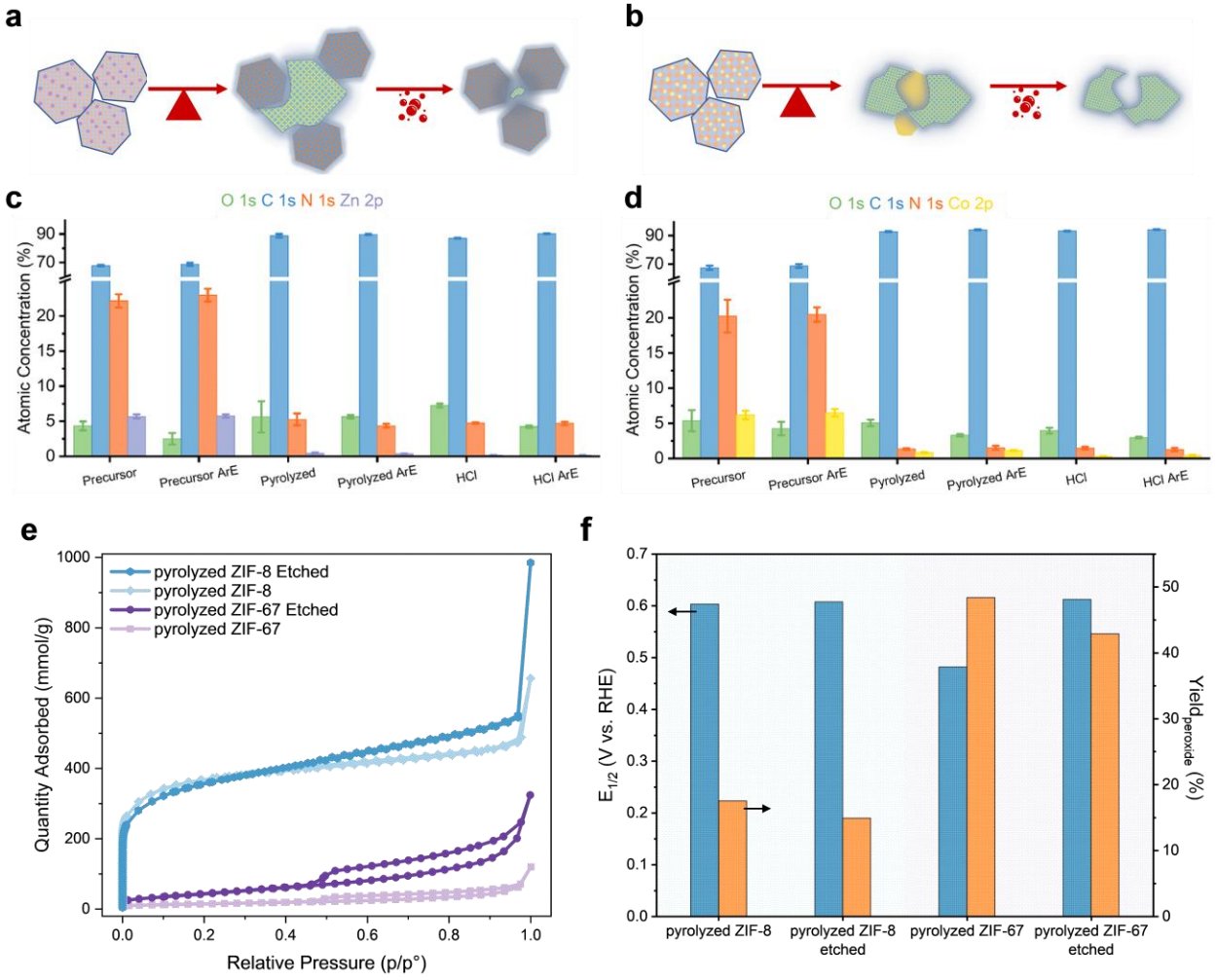

Figure 4. Comparison of pyrolyzed ZIF-8 and ZIF-67 before and after acid etching. Samples were pyrolyzed to 975 °C.

a-b. A schematic of transformations of precursors during pyrolysis and acid etching of ZIF-8 (a) and ZIF-67 (b)

c. Atomic concentration of different elements gained from XPS of ZIF-8, pyrolyzed ZIF-8 before and after acid etching (HCl), as well as acid etching after Ar beam etching (HCl ArE).

d. Atomic concentration of different elements gained from XPS of ZIF-67, pyrolyzed ZIF-67 before and after acid etching (HCl), as well as acid etching after Ar beam etching (HCl ArE).

e. Adsorption isotherm plots of N_2 on the pyrolyzed ZIF-8 and ZIF-67 before and after acid etching (980 °C)

f. Half-wave potential (blue bar) and peroxide yield (orange bar) gained from RRDE experiment for the pyrolyzed sample before and after acid etching. Disk and ring current density were collected under 1600 rpm rotating speed. The sample loading on the electrode was of 800 µg cm^{-2}_{geo} and the electrode surface was of 0.247 cm^2. The electrolyte is O_2-saturated 0.1 M $HClO_4$.

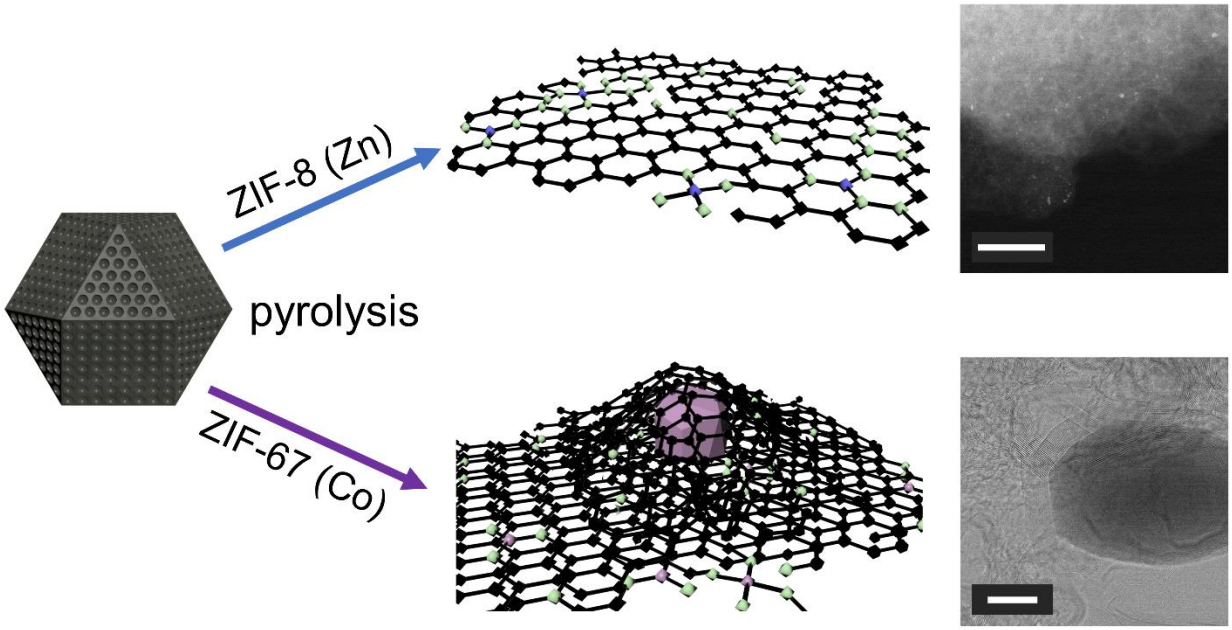

Figure 5. Schematic figure on pyrolyzing ZIF-8 and ZIF-67 to over 1000 ºC.

Blue, purple, green, and black spheres represent Zn, Co, N and C atoms/clusters/particle, respectively.

The TEM on top is the Zn-MOF pyrolyzed to 1050 ºC and cold down under vacuum. The TEM at the bottom is the ZIF-67 pyrolyzed to 1050 ºC under vacuum. The scale bars on both TEM images are 10 nm.